IEEE Access
Multidisciplinary ⋮ Rapid Review ⋮ Open Access Journal

Received May 27, 2021, accepted June 23, 2021, date of publication June 28, 2021, date of current version July 6, 2021.
Digital Object Identifier 10.1109/ACCESS.2021.3093098

Improved Numerical-Analytical Thermal Modeling Method of the PCB With Considering Radiation Heat Transfer and Calculation of Components' Temperature

YABIN ZHANG
School of Electrical Engineering and Electronic Information, Xihua University, Chengdu, Sichuan 610039, China
e-mail: 1220170062@mail.xhu.edu.cn

This work was supported by the Sichuan Science and Technology Program under Grant 2020YFG0152.

This work did not involve human subjects or animals in its research.

ABSTRACT The previous work relating to the numerical-analytical coupling method for steady-state thermal analysis of the laminated PCB structure is first briefly reviewed. The Fourier-series analytical solution of temperature and the finite volume method were linked together for thermally modeling the PCB. For further modeling the PCB with components, thermal-resistance parameters of the components are then used for correlating components' temperatures with the variable arrays in the coupling equations. For further considering radiation heat transfer between the PCB and the ambient, an iterative method is proposed. The radiation-equivalent heat transfer coefficient for each surface cell and each component can be updated during the iteration. Moreover, for improving the efficiency, the multigrid strategy is integrated in the coupling method for generating discrete cells of three levels in the metal layer and PCB surface region. To testify the iterative method, the model of a simple one-layer structure is compared with that built in COMSOL Multiphysics. The modeling results of the PCB of a phantom DC-DC power supply under radiation heat transfer are also given and discussed, and the modeling accuracy is approximately derived based on Richardson's extrapolation.

INDEX TERMS Thermal modeling of the PCB, radiation heat transfer, Fourier-series analytical solution, finite volume method, multigrid method, iterative method, thermal resistance of components.

I. INTRODUCTION

Thermal modeling of the PCB has been considered as an effective way to evaluate the capability of thermal diffusion of the PCB and to estimate components' temperature [1]–[14]. Historically, some modeling methods of analyzing the effective thermal conductivity of the PCB structure were investigated, such as the method of deriving the lumped thermal conductivity of the PCB [1], [2] and the method of deriving the discrete thermal conductivity of orthogonal anisotropy (x, y, z direction in Cartesian coordinate) based on the PCB wiring diagram [3], [4]. In recent years, equivalent thermal-resistance models of the PCB [5]–[7] have been also researched. Two analytical thermal-resistance models and design optimization methods were proposed for optimizing the layout of PCB vias and thermal pads under the IC [5]. Based on the layerwise equivalent thermal resistance of the nanosatellite PCB, both the detailed and simplified modeling methods for thermal analysis of the PCB have been typically proposed [6], [7].

On the other hand, FloTHERM from Mentor and Icepak from ANSYS were also developed for PCB thermal-simulation. FloTHERM is mainly based on the effective thermal conductivity that relates to the copper-coverage rate in the PCB and the empirical method according to the analysis of over 140 PCB configurations [8], [9]. But such method may result in slightly over-estimating the temperature of the component [9].

Icepak is based on the Finite Element Method (FEM). The FEM-based software is generally considered as having

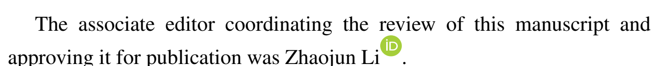

The associate editor coordinating the review of this manuscript and approving it for publication was Zhaojun Li.

This work is licensed under a Creative Commons Attribution-NonCommercial-NoDerivatives 4.0 License.
For more information, see https://creativecommons.org/licenses/by-nc-nd/4.0/

higher calculation accuracy, but often the structure must be wholly discretized, which may influence the operation efficiency [10].

The thermal modeling method introduced in this paper was first proposed [11], [12] based on coupling the Fourier-series analytical solution of temperature and the FVM (Finite Volume Method)-based discretization. With such coupling method, the laminated PCB structure is not necessary to be wholly discretized, but only the metal layer and surface region. The electrical-thermal analysis of Joule heating in PCB tracks was included as well [11]–[13]. A test solver based on the coupling method was first developed in MATLAB with the uniform grid in Cartesian coordinate [12], [13]. The precision of the coupling method has been verified through the modeling comparison with COMSOL [12]–[14]. In Section II, a brief introduction of the coupling method is given.

However, the operation efficiency of the modeling method was significantly influenced by the uniform-grid numerical discretization. Hence, the multigrid method is applied. In Section III, generation steps of the three-level multigrid and possible adjacent scenarios of three-level metal cells are explained.

On the other hand, thermal-resistance parameters of components are used for taking into account components' coverage and their contribution to the heat spreading in the PCB as well as estimating their temperatures. The components' temperatures are correlated with the variable arrays of temperature and heat flux in the coupling matrix equations. The corresponding mathematical processing is presented in Section IV.

The Fourier-series analytical solution of temperature was mainly derived based on the assumed average heat transfer coefficient (HTC) of the PCB surface [13], [14]. But under such simplified assumption, radiation heat transfer cannot be directly analyzed in the model. Hence, as another improvement, an iterative method for correlating the HTC and radiation heat transfer is discussed in Section V. Compared with the COMSOL model, the verification of the method is given in Section VI.

The PCB of a phantom DC-DC power supply was modeled with the improved coupling method. The circuit and PCB were automatically generated by the online tool TI WEBENCH@Power Supply. Thermal parameters and three-level discrete map of the PCB can be found in the first part of Section VII, where the comparison of operation burden between the uniform grid and multigrid can be found as well. In the second part of Section VII, the modeling results are given and analyzed. The accuracy of the modeling results is also discussed and approximately derived based on Richardson's extrapolation.

II. PREVIOUS WORK OF THE NUMERICAL-ANALYTICAL COUPLING METHOD FOR STEADY-STATE THERMAL ANALYSIS OF THE PCB STRUCTURE

Discretizing the whole structure is a shortcoming in numerical methods [10], [15], [16]. Instead, the classic Fourier-series method [12]–[14], [17]–[21] has immunity to the aspect ratio between the whole structure and heat sources, so that the structure is usually not necessary to be fully discretized and only the temperature distribution of expected regions or points have to be solved.

The Fourier-series analytical solution used in the coupling method was first derived for developing the analytical thermal-solver 'DJOSER' [17], [18], which was used for thermal analysis of power devices. In recent years, the classic analytical method has been still applied for establishing thermal models of the SiC module [19] and GaN device [20], as well as the jet-impingement cooling of a microprocessor chip [21]. Compared to the FEM, higher computational efficiency of the analytical solution was testified [20], [21], and easier integration with optimization tools for microelectronics can be obtained [21].

In the coupling method, the analytical solution was applied first for the insulating layer in the core of the PCB based on Cartesian coordinate [13], [14]. The Finite Volume Method (FVM) was then applied for taking into account the non-homogeneity of the core structure, especially the heat-spreading contribution of metal layers and vias [12], [13].

FIGURE 1. Structure schematic of a rectangular PCB with one core.

A. ANALYTICAL SOLUTION

Due to high thermal conductivity and μm-level thickness, the temperature differences between the top and bottom surfaces of the metal layer are approximately ignored in the coupling method. Hence, for the kind of PCB structure with one core and two metal layers as shown in Fig. 1, the heat transfer between the core and the ambient can be approximately equivalent to that between the insulating layer and the ambient. On the other hand, the lateral heat-spreading contribution of the vias is mostly limited by the surrounding insulating material, and vias' contribution to the thermal conduction between metal layers are taken into account in the numerical analysis [12]–[14]. Hence, the insulating layer can be first assumed to be homogenous, and the governed equation for steady-state heat transfer of the insulating layer can be expressed as follows:

$$\nabla^2 T = 0 \tag{1}$$

in which, T is the temperature variation compared with the ambient temperature. The temperature distributions of both the top and bottom sides can represent respectively that of the attached metal layers, and thus are usually expected to be derived. Thermal boundary conditions of the insulating layer

can be simplified as follows:

$$\begin{cases} \frac{\partial T}{\partial x} = 0, \{x = 0, x = L_x\} \; \frac{\partial T}{\partial y} = 0, \\ \quad \{y = 0, y = L_y\} \\ -k_i \frac{\partial T}{\partial z} = q_{iu}(x, y) - h_u T \; \{z = 0\}, \\ \quad -k_i \frac{\partial T}{\partial z} = q_{id}(x, y) + h_d T \; \{z = L_{in}\} \end{cases} \tag{2}$$

in which, L_x, L_y, and L_{in} are the layer lengths along three axes respectively; k_i is the thermal conductivity of the layer; $q_{iu}(x,y)$ is the distribution of the vertical (z-axis) heat flux transferred from the top side, whereas similarly $q_{id}(x,y)$ is defined for the bottom side; h_u and h_d are the average HTCs that approximately represent the heat transfer from the top and bottom sides to the ambient respectively. The thermal resistance of the solder mask can be also taken into account in the HTC. Adiabatic condition is assumed at thin edges of the layer.

The upper double-side equation can be considered as the superposition of the topside and bottom-side groups:

$$\begin{cases} T = \theta + \eta \\ \begin{cases} \nabla^2 \theta = 0 \\ \frac{\partial \theta}{\partial x} = 0 \{x = 0, x = L_x\}, \quad \frac{\partial \theta}{\partial y} = 0 \{y = 0, y = L_y\} \\ -k_i \frac{\partial \theta}{\partial z} = q_{iu}(x, y) - h_u \theta \; \{z = 0\}, \\ -k_i \frac{\partial \theta}{\partial z} = h_d \theta \; \{z = L_{in}\} \end{cases} \\ \begin{cases} \nabla^2 \eta = 0 \\ \frac{\partial \eta}{\partial x} = 0 \{x = 0, x = L_x\}, \quad \frac{\partial \eta}{\partial y} = 0 \{y = 0, y = L_y\} \\ -k_i \frac{\partial \eta}{\partial z} = -h_u \eta \; \{z = 0\}, \\ -k_i \frac{\partial \eta}{\partial z} = q_{id}(x, y) + h_d \eta \; \{z = L_{in}\} \end{cases} \end{cases} \tag{3}$$

in which, θ is the sub-variable of T under the only thermal contribution of $q_{iu}(x,y)$; η is the other sub-variable of T when $q_{id}(x,y)$ is only considered.

The analytical solution of each group can be expressed in the form of Fourier series. For example, for the top-side group, θ can be expressed as:

$$\begin{cases} \theta = C_1 z + C_2 +_{(n \neq m = 0)} \sum_{n=0}^{\infty} \sum_{m=0}^{\infty} C_{n,m} \cos(\beta_n x) \\ \quad \times \cos(\mu_m y)(sh(\gamma_{n,m} z) + C_{\gamma_{n,m}} ch(\gamma_{n,m} z)) \\ \beta_n = n\pi / L_x, \; \mu_m = m\pi / L_y \end{cases} \tag{4}$$

in which, β_n, μ_m, and $\gamma_{n,m}$ are the eigenvalues in the series; n and m are ordinal numbers; C_1, C_2, $C_{n,m}$, and $C\gamma_{n,m}$ are the coefficients. By substituting (4) in the topside thermal boundary conditions, several coefficients can be derived:

$$\begin{cases} C_2 = -C_1 (\frac{1}{H_d} + L_{in}) \\ C_{\gamma_{n,m}} = -\frac{H_d sh(\gamma_{n,m} L_{in}) + \gamma_{n,m} ch(\gamma_{n,m} L_{in})}{H_d ch(\gamma_{n,m} L_{in}) + \gamma_{n,m} sh(\gamma_{n,m} L_{in})} \\ H_d = {h_d}/{k_i}, \; H_u = {h_u}/{k_i} \end{cases} \tag{5}$$

in which, H_d and H_u are the intermediate constants.

Next, by substituting (4) into the condition at top surface ($z = 0$) and applying Fourier integration method, other coefficients can be derived as (6), as shown at the bottom of the next page.

in which, $q_{iu,i}$ refers to the approximate uniform heat flux in the ith square discrete region; d_q is the edge length of each discrete region; δ_m and δ_n are constant coefficients (7), as shown at the bottom of the next page.

Finally, as shown in (7), the analytical solution of θ at any expected position in the insulating layer can be expressed in the product form of the array $R_u(x,y,z)$ of thermal-resistance kind and q_u, the array form of $q_{iu}(x,y)$. $C'_{qiu,i}$ is the cell coefficient of the array $R_u(x,y,z)$; N_1 is the number of discrete regions; C'_1 is the z-dependent coefficient including both C_1 and C_2; $C_{n,m,qiu,i}$ is the cell coefficient for deriving $C'_{qiu,i}$; n and m are the ordinal numbers of eigenvalues; N_e is the number of eigenvalue groups. In the similar way, the analytical solution of η at any expected position in the insulating layer can be derived under the only thermal contribution of $q_{id}(x,y)$.

Therefore, based on the analytical solution, the temperature distribution on both the top and bottom surfaces of the insulating layer can be expressed in the form of matrix equations:

$$\begin{cases} T_u = \theta_u + \eta_u = R_{u,u} q_u + R_{u,d} q_d \\ T_d = \theta_d + \eta_d = R_{d,u} q_u + R_{d,d} q_d \\ \theta_u = R_{u,u} q_u \\ \eta_u = R_{u,d} q_d \\ \theta_d = R_{d,u} q_u \\ \eta_d = R_{d,d} q_d \end{cases} \tag{8}$$

in which, the arrays T_u and T_d denote respectively the temperature distribution on the top and bottom surfaces; θ_u and η_u are the sub-variables of T_u; θ_d and η_d are the sub-variables of T_d; q_d is the array form of $q_{id}(x,y)$; $R_{u,u}$ refers to the coefficient matrix relating to T_u and q_u; $R_{u,u} q_u$ represents the thermal effect of q_u to the top surface; in the similar way, $R_{d,u} q_u$ represents the thermal effect of q_u to the bottom surface; $R_{u,d} q_d$ and $R_{d,d} q_d$ represent respectively the thermal effect of q_d to the top and bottom surfaces.

B. NUMERICAL-ANALYTICAL MODELING STRATEGY CONSIDERING THE HEAT SPREADING IN METAL LAYERS

Due to much higher thermal conductivity of the material of the metal layer compared to that of the insulating layer, the heat spreading through metal layers and the vertical

thermal conduction through vias cannot be neglected. The FVM [16] under Cartesian coordinate was integrated for discretizing the metal layer into a number of cells, so that the heat spreading can be approximately described through the truncation of Taylor series with 2nd order precision [14], [16].

The steady-state heat transfer equation for a discrete cell in the metal layer as shown in Fig. 2 can be expressed in the form of Poisson's equation:

$$\frac{\partial^2 T}{\partial x^2}+\frac{\partial^2 T}{\partial y^2}+\frac{\partial^2 T}{\partial z^2}+\frac{q_J}{k_m}=0 \tag{9}$$

$$\begin{cases} C_1=-\dfrac{d_q^2*(q_{iu,1}+\cdots+q_{iu,N_1})}{k_iL_xL_y[1+H_u(L_{in}+{}^1/_{H_d})]} \\ C_{n,m}=-\dfrac{\sum_{i=1}^{N_1}2q_{iu,i}(2-\delta_n-\delta_m)\iint_{S_{q_{iu,i}}}\cos(\beta_n\cdot x)\cos(\mu_m\cdot y)dxdy}{k_iL_xL_y[\gamma_{n,m}+H_u\frac{\gamma_{n,m}ch(\gamma_{n,m}L_{in})+H_d sh(\gamma_{n,m}L_{in})}{\gamma_{n,m}sh(\gamma_{n,m}L_{in})+H_d ch(\gamma_{n,m}L_{in})}]} \\ \delta_m=\begin{cases}1, & m=0\\ 0, & m\neq 0\end{cases},\ \delta_n=\begin{cases}1, & n=0\\ 0, & n\neq 0\end{cases} \end{cases} \tag{6}$$

$$\begin{cases} \theta(x,y,z)=C_1'\begin{pmatrix}1 & 1 & \cdots & 1\end{pmatrix}\begin{pmatrix}q_{iu,1}\\ q_{iu,2}\\ \vdots\\ q_{iu,N_1}\end{pmatrix}+\begin{pmatrix}C_{q_{iu,1}} C_{q_{iu,2}}\cdots C_{q_{iu,N_1}}\end{pmatrix}\begin{pmatrix}q_{iu,1}\\ q_{iu,2}\\ \vdots\\ q_{iu,N_1}\end{pmatrix}=\begin{pmatrix}C'_{q_{iu,1}} C'_{q_{iu,2}}\cdots C'_{q_{iu,N_1}}\end{pmatrix}q_u=R_u(x,y,z)q_u \\ R_u(x,y,z)=\begin{pmatrix}C'_{q_{iu,1}} & C'_{q_{iu,2}} & \cdots & C'_{q_{iu,N_1}}\end{pmatrix}=\begin{pmatrix}C_1'\\ \cos(\beta_1\cdot x)\cos(\mu_0\cdot y)\\ \vdots\\ \cos(\beta_{N_e}\cdot x)\cos(\mu_0\cdot y)\\ \cos(\beta_0\cdot x)\cos(\mu_1\cdot y)\\ \vdots\\ \cos(\beta_0\cdot x)\cos(\mu_{N_e}\cdot y)\\ \vdots\\ \cos(\beta_{N_e}\cdot x)\cos(\mu_{N_e}\cdot y)\end{pmatrix}^{-1} \\ \quad\times\begin{pmatrix}1 & 1 & \cdots & 1\\ C_{1,0,q_{iu,1}} & C_{1,0,q_{iu,2}} & \cdots & C_{1,0,q_{iu,N_1}}\\ \vdots & \vdots & & \vdots\\ C_{N_e,0,q_{iu,1}} & C_{N_e,0,q_{iu,2}} & \cdots & C_{N_e,0,q_{iu,N_1}}\\ C_{0,1,q_{iu,1}} & C_{0,1,q_{iu,2}} & \cdots & C_{0,1,q_{iu,N_1}}\\ \vdots & \vdots & & \vdots\\ C_{0,N_e,q_{iu,1}} & C_{0,N_e,q_{iu,2}} & \cdots & C_{0,N_e,q_{iu,N_1}}\\ \vdots & \vdots & & \vdots\\ C_{N_e,N_e,q_{iu,1}} & C_{N_e,N_e,q_{iu,2}} & \cdots & C_{N_e,N_e,q_{iu,N_1}}\end{pmatrix} \\ C_1'=\dfrac{d_q^2*(-z+\frac{1}{H_d}+L_{in})}{k_iL_xL_y[1+H_u(L_{in}+{}^1/_{H_d})]} \\ C_{n,m,q_{iu,i}}=-(sh(\gamma_{n,m}z)+C_{\gamma_{n,m}}ch(\gamma_{n,m}z))\dfrac{2(2-\delta_n-\delta_m)\iint_{S_{q_{iu,i}}}\cos(\beta_n\cdot x)\cos(\mu_m\cdot y)dxdy}{k_iL_xL_y[\gamma_{n,m}+H_u\frac{\gamma_{n,m}ch(\gamma_{n,m}L_{in})+H_d sh(\gamma_{n,m}L_{in})}{\gamma_{n,m}sh(\gamma_{n,m}L_{in})+H_d ch(\gamma_{n,m}L_{in})}]} \end{cases} \tag{7}$$

in which, q_J is the volume density of Joule-heating rate and k_m is the thermal conductivity of the metal material.

By integrating (9) and applying Gauss's divergence theorem, we can further derive the following integration of six surfaces of the central cell shown in Fig. 2:

$$\int (q_e dA - q_w dA + q_n dA - q_s dA + q_u dA - q_d dA) = -q_c l_c^2 d_m \tag{10}$$

in which, l_c is the edge length; A is the variable of surface area; d_m is the thickness of the cell; q_c is the volume density of Joule-heating rate in the cell; q_u is the heat flux transferred from the top and usually represents the heat flux transferred from the components through pins or pads; q_d is the net heat flux transferred to the insulating layer; q_e, q_w, q_n and q_s are the heat flux normal to four side surfaces respectively.

By applying the central difference approximation method [16], the integration form (10) of the governed equation can be further simplified in (11), as shown at the bottom of the page, through the truncation of Taylor series with second-order precision. As shown in Fig. 2, T_E, T_W, T_N and T_S denote the temperatures of four adjacent cells respectively. If the central metal cell is connected with another metal layer through a via, there will be another part of the heat flux through the via as shown in (11). $\psi_{Nv,z}$ denotes the thermal resistance through the via, and $T_{C,dv}$ denotes the temperature of the connected metal cell in the other metal layer.

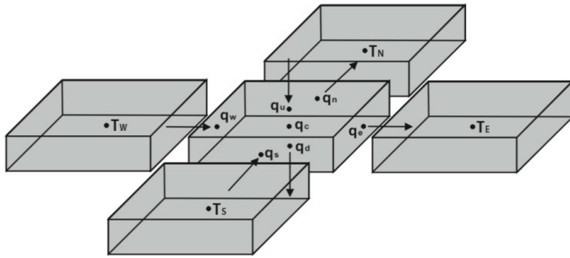

FIGURE 2. Schematic of the heat transfer through discrete cells in the metal layer.

As similar to the processing of the analytical solution, the heat-spreading equation (11) for each metal cell can be summarized together in the form of matrix equations:

$$\begin{cases} M_{M,u}T_{M,u} - M_{V,d}T_{M,d} = q_{MJ,u} - q_{M,u} \\ M_{M,d}T_{M,d} - M_{V,u}T_{M,u} = q_{MJ,d} - q_{M,d} \end{cases} \tag{12}$$

in which, subscripts u and d refer to the top and bottom sides respectively; subscript M refers to the metal layer; subscript V refers to the metal cell connected through the via; M_M denotes the coefficient matrix that gathers all the coefficients of temperature variables in each heat-spreading equation of one metal layer, whereas M_V is the coefficient matrix relating to temperature variables of the cells of the other layer connected through vias; q_{MJ} denotes the array of the heat flux relating to q_c and q_u; q_M denotes the array of the heat flux relating to q_d and represents the heat flux transferred from the metal layer to the insulating layer.

Since the temperature difference between the top side and bottom side of a metal cell is neglected, the temperature of a metal cell can refer to the temperature of the attached region of the insulating layer. Hence, the temperature distribution in the metal layer can be also expressed in the form of the analytical solution like (8):

$$\begin{cases} T_{M,u} = R_{Mu,Mu}q_{M,u} + R_{Mu,Md}q_{M,d} \\ T_{M,d} = R_{Md,Mu}q_{M,u} + R_{Md,Md}q_{M,d} \end{cases} \tag{13}$$

in which, subscript Mu and Md refer to the top and bottom metal layers respectively; $R_{Mu,Mu}$ refers to the coefficient matrix relating to $T_{M,u}$ and $q_{M,u}$; $R_{Mu,Mu}q_{M,u}$ represents the thermal effect of $q_{M,u}$ to the attached insulating region of the top metal layer; in the similar way, $R_{Md,Mu}q_{M,u}$ represents the thermal effect of $q_{M,u}$ to the bottom attached insulating region; $R_{Mu,Md}q_{M,d}$ and $R_{Md,Md}q_{M,d}$ represents the thermal effect of q_d to the attached insulating region on the top and bottom sides respectively. Moreover, by combining (13) and (12), the group of equations for deriving the temperature distribution in metal layers can be constructed:

$$\begin{cases} T_{M,u} = R_{Mu,Mu}q_{M,u} + R_{Mu,Md}q_{M,d} \\ T_{M,d} = R_{Md,Mu}q_{M,u} + R_{Md,Md}q_{M,d} \\ M_{M,u}T_{M,u} - M_{V,d}T_{M,d} = q_{MJ,u} - q_{M,u} \\ M_{M,d}T_{M,d} - M_{V,u}T_{M,u} = q_{MJ,d} - q_{M,d} \end{cases} \tag{14}$$

Hence, four unknown arrays $T_{M,u}$, $T_{M,d}$, $q_{M,u}$, and $q_{M,d}$ can be solved from the group of equations.

The integration of the FVM-based numerical analysis of the heat spreading in metal layers also represents the consideration of the thermal influence of the metal layer to the insulating layer, as including a complement thermal boundary condition of the insulating layer. Based on the coupling method, several one-layer and two-layer PCB models were built and acceptable accuracies were verified after comparing with COMSOL models [12]–[14].

III. THREE-LEVEL MULTIGRID

However, in the previous coupling strategy, the metal layer and other surface regions were discretized based on the regular grid of uniform density. The number of discrete cells was

$$k_m d_c d_m \left(\frac{T_c - T_E}{d_c} - \frac{T_W - T_c}{d_c} + \frac{T_c - T_N}{d_c} - \frac{T_S - T_c}{d_c}\right) + \frac{T_c - T_{c,dv}}{\psi_{Nv,z}} = q_c d_c^2 d_m + q_u d_c^2 - q_d d_c^2$$

$$\Rightarrow \left(\frac{4k_m d_m}{d_c^2} + \frac{1}{\psi_{Nv,z}}\right)T_c - \frac{k_m d_m}{d_c^2}(T_E + T_W + T_N + T_S) - \frac{T_{c,dv}}{\psi_{Nv,z} d_c^2} = q_c d_m + q_u - q_d \tag{11}$$

directly equal to the number of pixels of the corresponding region in the layout map. Hence, when the resolution of the layout map was relatively high, the uniform grid usually led to a large number of cells, which formed a huge computation burden.

In order to improve the operation efficiency, the multigrid method can be applied. With multiple densities in the grid, the multigrid can significantly reduce the number of discrete cells, and thus has been widely applied for computational thermal analysis of ICs [22], [23].

The uniform grid has been substituted by a three-level multigrid. There are three steps for generating the multigrid. The level-1 grid is first generated in the same way as the one-level uniform grid, thus having the same density as the layout map. Then each group of four adjacent cells that are able to form a bigger square cell are unified to generate the grid of level-2. Since the density of heat spreading could be much higher in the cells of the footprint pad or under the components, such cells are not unified during the generation of the level-2 grid. Last, in the similar way, the cells in the level-3 grid are generated by unifying the cells of the level-2 grid. A schematic of the three-level multigrid is shown in Fig. 3.

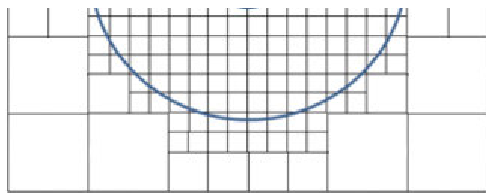

FIGURE 3. Schematic of the three-level multigrid.

Under the three-level multigrid, the calculation for the coefficients given in (7) has to depend on the actual size of the cells. On the other hand, when some metal cells of different sizes are adjacent to each other, in the corresponding heat-spreading equation (11) of each adjacent cell, some coefficients describing the thermal-conductance between cells have to be modified too. Hence, after generating the multigrid the surrounding scenario of each metal cell has to be identified.

First, as shown in Fig. 4 a cell is possible to be surrounded by the cells of the same type. In summary, there is only 1 possible scenario when the cell is surrounded by four cells of the same size; there are 4 possible scenarios (PS) when the cell is surrounded by three cells of the same size; there are 6 PS when the cell is surrounded by two cells of the same size; and there are 4 PS when the cell is attached by only one cell of the same size.

Second, as shown in Fig. 5 one cell is possible to be surrounded by the cells of 4 times bigger. In summary, there are 8 PS when the cell is only attached by one cell of 4 times bigger; there are 4 PS when the cell is surrounded by two cells of 4 times bigger.

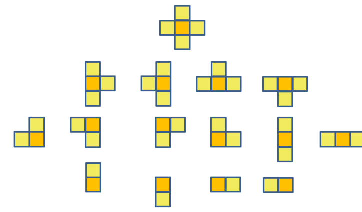

FIGURE 4. Possible scenarios for a cell surrounded by the cells of the same type.

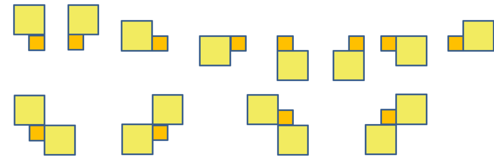

FIGURE 5. Possible scenarios for a cell surrounded by the cells of 4 times bigger.

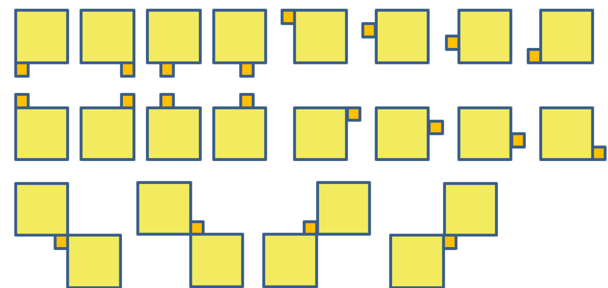

FIGURE 6. Possible scenarios for a cell surrounded by the cells of 16 times bigger.

Third, similarly as shown in Fig. 6 one cell is possible to be surrounded by the cells of 16 times bigger. After searching for all the PS mentioned above, the surrounding scenarios for each metal cell can be found.

IV. CORRELATING COMPONENTS' TEMPERATURES WITH THE VARIABLES IN COUPLING EQUATIONS

As shown in (2), two average HTCs were assumed for respectively simplifying the thermal boundary conditions of the top and bottom PCB surfaces in the coupling method. However, the fact is that some surface regions are covered by the components and do not exchange heat directly with the ambient. Hence, the influence of components' coverage on the thermal distribution of the PCB structure was not taken into account, and the temperature information of the components was not possible to be solved. On the other hand, the contribution of thermal conduction of the component to the heat spreading in the PCB cannot be analyzed either.

In order to correct the assumed boundary conditions, on one hand, the non-existent heat exchange represented by the average HTC for the area occupied by components can be compensated by considering such flux as the extra heat flux transferred into the area. For example, for a cell covered by the component on the top surface, the extra compensated

heat flux can be expressed as the product of the HTC h_u and cell temperature T_C:

$$q_{ex} = h_u T_C \tag{15}$$

On the other hand, thermal-resistance parameters of the components can be used for calculating the thermal conduction between the PCB and component junction, as well as between the ambient and components. One parameter is the total thermal resistance between the junction and bottom footprint pads (or pins), and can be usually denoted by $R_{\theta JC}$ or $R_{\theta JC(bot)}$ [24]. The pads (or pins) as a part of the metal layer can be discretized numerically, thus the average thermal resistance between the junction and each discretized pad (or pin) cell of one component can be calculated as follows:

$$R_{\theta JC,pc} = N_{pc} R_{\theta JC} \tag{16}$$

in which, N_{pc} is the number of pad (or pin) cells of the component. Then the temperature difference between the junction and the mth pad (or pin) cell can be described as:

$$T_J - T_{pc,m} = P_{pc,m} R_{\theta JC,pc} \tag{17}$$

in which, $P_{pc,m}$ refers to the rate of heat transfer between them.

Another thermal-resistance parameter is the total thermal resistance between the junction and case top of a component, and is usually denoted by $R_{\theta JC(top)}$ [24]. $R_{\theta JC(top)}$ can be used for deriving the rate of heat transfer from the case top to the ambient, denoted by P_{top}. The product of the HTC h_{top}, the area S_{top} and average temperature T_{top} of the case top can also represent P_{top}:

$$P_{top} = \frac{(T_J - T_{top})}{R_{\theta JC(top)}} = h_{top} S_{top} T_{top} \tag{18}$$

Then, the junction temperature T_J can be derived:

$$T_J = T_{top}(1 + h_{top} S_{top} R_{\theta JC(top)}) = T_{top} C_{top} \tag{19}$$

in which, C_{top} denotes the summarized constant coefficient.

Next, substitute T_J back in (17), $P_{pc,m}$ can be expressed as:

$$P_{pc,m} = \frac{(T_{top} C_{top} - T_{pc,m})}{R_{\theta JC,pc}} \tag{20}$$

Obviously, the sum of $P_{pc,m}$ of all pad (or pin) cells and P_{top} is equal to the total heating power generated by the component:

$$\begin{aligned} P_h &= P_{top} + \sum_{m=1}^{N_{pc}} P_{pc,m} \\ &= h_{top} S_{top} T_{top} + T_{top} \sum_{m=1}^{N_{pc}} \frac{C_{top}}{R_{\theta JC,pc}} - \sum_{m=1}^{N_{pc}} \frac{T_{pc,m}}{R_{\theta JC,pc}} \end{aligned} \tag{21}$$

Furthermore, T_{top} can be derived and substituted back in (20) to express $P_{pc,m}$ using the temperature of each pad (or pin) cell $T_{pc,m}$:

$$T_{top} = \frac{(P_h + \sum_{m=1}^{N_{pc}} \frac{T_{pc,m}}{R_{\theta JC,pc}})}{(h_{top} S_{top} + \sum_{m=1}^{N_{pc}} \frac{C_{top}}{R_{\theta JC,pc}})} = \frac{(P_h + \sum_{m=1}^{N_{pc}} \frac{T_{pc,m}}{R_{\theta JC,pc}})}{C_{top,Npc}} \tag{22}$$

$$\begin{aligned} P_{pc,m} &= \frac{(T_{top} C_{top} - T_{pc,m})}{R_{\theta JC,pc}} \\ &= \frac{P_n C_{top}}{C_{top,Npc} R_{\theta JC,pc}} - \frac{\sum_{m=1}^{N_{pc}} \frac{T_{pc,m}}{R_{\theta JC,pc}} C_{top}}{C_{top,Npc} R_{\theta JC,pc}} - \frac{T_{pc,m}}{R_{\theta JC,pc}} \end{aligned} \tag{23}$$

in which, $C_{top,Npc}$ denotes the summarized constant coefficient representing the denominator of the expression of T_{top}. Then $P_{pc,m}$ and q_{ex} of each pad (or pin) cell can be included in the array q_{MJ} of (12), and the terms with $T_{pc,m}$ in the expression of $P_{pc,m}$ can be further correlated to the temperature array T_M of the corresponding metal layer:

$$\begin{cases} M_{M,u} T_{M,u} - M_{V,d} T_{M,d} = q_{MJ,u} - q_{M,u} \\ M_{M,d} T_{M,d} - M_{V,u} T_{M,u} = q_{MJ,d} - q_{M,d} \\ q_{MJ,u} = q_{P,u} + M_{R,u} T_{M,u} + M_{Mcov-u} T_{M,u} \\ q_{MJ,d} = q_{P,d} + M_{R,d} T_{M,d} + M_{Mcov-d} T_{M,d} \end{cases} \tag{24}$$

in which, subscripts u and d still refer to the top and bottom sides respectively; the array q_P relates to the first constant term in the expression of $P_{pc,m}$ for each pad (or pin) cell of a component and the Joule-heat rate in metal cells; the coefficient matrix M_R relates to the coefficients of $T_{pc,m}$ in the second and third terms in the expression of $P_{pc,m}$; subscripts *Mcov-u* and *Mcov-d* refer to the covered regions of the top and bottom metal layers respectively; $M_{Mcov-u} T_{M,u}$ represents the array including the compensated heat flux q_{ex} for the metal cells on the top side covered by the component; the term $M_{Mcov-d} T_{M,d}$ is thus relating to the covered metal cells on the bottom side; other coefficients or arrays keep the same meanings respectively as explained for (12).

Due to the existence of metal pads or pins, the covered region usually does not contact with the component but is separated from the component by a slim "air film". Hence, such region can be approximately considered thermally insulated to the component due to the much higher thermal resistance of the "film" compared to $R_{\theta JC}$. The heat transferred between components and the PCB can be thus assumed only through metal pads or pins. Moreover, in order to take into account q_{ex} for the covered insulating region, the corresponding temperature distribution of the region has to be the new unknown variable in the group of coupling equations.

Therefore, the group of matrix equations for the coupling solution can be further updated to the form shown in (25), as shown at the bottom of the next page. In the group equations, first four equations relate to the analytical solution;

the subscripts *Icov-u* and *Icov-d* refer to the covered insulating regions on the top and bottom sides respectively; the subscripts *Mcov-u, Mcov-d, u, d, Mu* and *Md* keep the same meanings respectively as before; the product of the coefficient matrix M_{Icov-u} and T_{Icov-u} refers to the array $q_{ex,Icov-u}$, which is relating to q_{ex} of the covered insulating region on the top side; $q_{ex,Icov-d}$ is defined and expressed in the similar way of $q_{ex,Icov-u}$; $q_{ex,Icov-u}$ or $q_{ex,Icov-d}$ is further multiplied with the corresponding matrix coefficient R to represent their thermal contribution to the corresponding analytical solution of the temperature distribution.

In this way, the temperatures of the component junction and case top, as well as the heat transfer between the component and the ambient, are correlated with the temperatures of pad (or pin) cells and can be derived after solving the temperature distribution of the metal layer. The influence of components' coverage is also considered. Hence, the PCB structure and components as a whole can be thermally modeled and analyzed.

V. AN ITERATIVE METHOD FOR CONSIDERING RADIATION HEAT TRANSFER

According to Stefan-Boltzmann law, when not exposed to the sun, the density of the net rate of radiation heat transfer of a surface can be expressed as follows:

$$q_r = \varepsilon\sigma(T_S^4 - T_a^4) \tag{26}$$

in which, ε denotes the emissivity of the surface; σ denotes Stefan-Boltzmann constant; T_s denotes the absolute temperature of the surface; T_a denotes the absolute temperature of the ambient. But such nonlinear relation cannot be directly taken into account in the coupling modeling method. Nevertheless, after the PCB reaches thermal steady state, the numerically equivalent HTC relating to the steady-state radiation heat transfer for each discrete surface cell or each component can be derived. Hence, if such kind of equivalent HTC is found, the non-linear relation of (26) will be possible to be converted to a linear boundary condition:

$$q_r = \varepsilon\sigma(T_S^4 - T_a^4) = h_e(T_S - T_a) \tag{27}$$

in which, h_e denotes the radiation-equivalent HTC under thermal steady state.

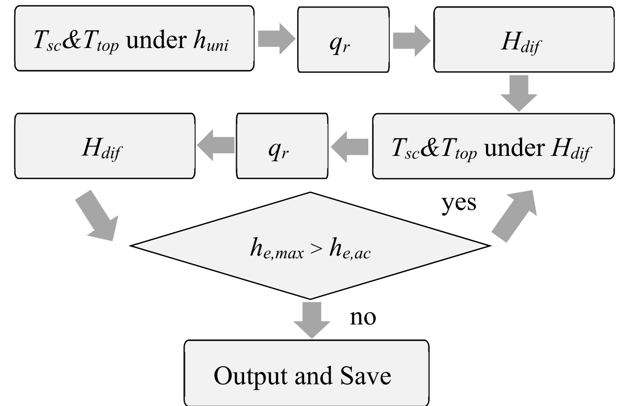

FIGURE 7. Iterative algorithm for deriving the radiation-equivalent HTC.

An iterative algorithm as shown in Fig. 7 is proposed for searching for the radiation-equivalent HTC of each component and each discrete cell under thermal steady state. In the block diagram, the temperature array of discrete cells T_{sc} and the array of the case-top temperature of components T_{top} are first derived under the hypothesis of a unique average HTC h_{uni} (such as h_u or h_d shown in (2)) of the PCB surface. Second, the array of the density of net radiation power from the corresponding PCB surface to the ambient, denoted by q_r, is approximately derived based on T_{sc} and T_{top}. In the third step, the radiation-equivalent HTC for each discrete cell and each component is calculated and its difference compared to h_{uni} is gathered in the array H_{dif}. Next, iterative calculations for T_{sc}, T_{top}, q_r, and H_{dif} are executed till the absolute maximum error of H_{dif} between two rounds of iteration, denoted by $h_{e,max}$, is no bigger than a preset acceptable error $h_{e,ac}$. The compensated HTC of the covered cell discussed in Section IV can be also included in H_{dif} as the constant element, but will not be the candidate for calculating $h_{e,max}$. Any specific emissivity of a cell or a component can be also set because the net radiation rate is calculated for each cell and component during the iteration.

With integration of the iterative method for radiation, the group of coupling equations (25) for the double-side PCB can be further updated to the form given in (28), as

$$\begin{cases} T_{M,u} = R_{Mu,Mu}q_{M,u} + R_{Mu,Md}q_{M,d} + R_{Mu,I\mathrm{cov}-u}q_{ex,I\mathrm{cov}-u} + R_{Mu,I\mathrm{cov}-d}q_{ex,I\mathrm{cov}-d} \\ T_{M,d} = R_{Md,Mu}q_{M,u} + R_{Md,Md}q_{M,d} + R_{Md,I\mathrm{cov}-u}q_{ex,I\mathrm{cov}-u} + R_{Md,I\mathrm{cov}-d}q_{ex,I\mathrm{cov}-d} \\ T_{I\mathrm{cov}-u} = R_{I\mathrm{cov}-u,Mu}q_{M,u} + R_{I\mathrm{cov}-u,Md}q_{M,d} + R_{I\mathrm{cov}-u,I\mathrm{cov}-u}q_{ex,I\mathrm{cov}-u} + R_{I\mathrm{cov}-u,I\mathrm{cov}-d}q_{ex,I\mathrm{cov}-d} \\ T_{I\mathrm{cov}-d} = R_{I\mathrm{cov}-d,Mu}q_{M,u} + R_{I\mathrm{cov}-d,Md}q_{M,d} + R_{I\mathrm{cov}-d,I\mathrm{cov}-u}q_{ex,I\mathrm{cov}-u} + R_{I\mathrm{cov}-d,I\mathrm{cov}-d}q_{ex,I\mathrm{cov}-d} \\ M_{M,u}T_{M,u} - M_{V,d}T_{M,d} = q_{MJ,u} - q_{M,u} \\ M_{M,d}T_{M,d} - M_{V,u}T_{M,u} = q_{MJ,d} - q_{M,d} \\ q_{MJ,u} = q_{P,u} + M_{R,u}T_{M,u} + M_{M\mathrm{cov}-u}T_{M,u} \\ q_{MJ,d} = q_{P,d} + M_{R,d}T_{M,d} + M_{M\mathrm{cov}-d}T_{M,d} \\ q_{ex,I\mathrm{cov}-u} = M_{I\mathrm{cov}-u}T_{I\mathrm{cov}-u} \\ q_{ex,I\mathrm{cov}-d} = M_{I\mathrm{cov}-d}T_{I\mathrm{cov}-d} \end{cases} \tag{25}$$

shown at the bottom of the page. The first four equations relate to the analytical solution; the fifth and sixth equations relate to the lateral heat spreading in metal layers; the seventh and eighth equations relate to the heat flux transferred from the components to the pads with consideration of the thermal resistance of components; subscript I refers to the insulating region not attached by the metal layer, whereas subscripts Iu and Id refer to such kind of region on the top and bottom sides respectively; q_{ex-r} refers to the array including the compensated heat flux for the discrete region due to components' coverage and radiation heat transfer; such compensated heat flux is represented by the product of the coefficient matrix M_{Hdif} and the corresponding temperature array; other subscripts, variables and coefficients keep the same meanings respectively as before. The unknown arrays include $T_{M,u}$, $T_{M,d}$, $T_{I,u}$, $T_{I,d}$, $q_{M,u}$, and $q_{M,d}$. In each round of iteration, the radiation-equivalent HTC for each discrete surface cell and each component can be updated. The iteration is running till the maximum difference of each HTC between two consecutive rounds is no bigger than the preset acceptable error $h_{e,ac}$.

VI. A ONE-LAYER MODEL FOR TESTING THE ITERATIVE METHOD

The test solver developed in MATLAB for the coupling method has been further improved based on the methods mentioned in previous sections. A simple one-layer FR-4 structure shown in Fig. 8 was modeled in both the test solver and COMSOL to test the mechanism and accuracy of the iterative method. The dimension of the board is 56mm × 63mm × 1.6mm. The yellow region refers to the metal layer of 35μm thick copper. The heat was assumed uniformly transferred into this region with the rate of 0.5W, thus the uniform heat flux is 4761.9W/m^2. The only way of heat transfer between the board and the ambient was assumed as the radiation from the top surface.

The emissivity through the top surface was assumed uniform and set to 0.9, which is approximately suitable for the epoxy-based solder mask [5] and the plastic package material of ICs [25], [26]. Based on the rule of generating three-level discrete cells introduced in Section III, the heating region

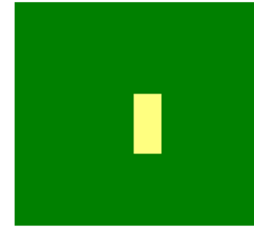

FIGURE 8. Layout of the simple one-layer structure.

was not discretized with the three-level multigrid, but only the green region. In the test solver, the layout map with the resolution of 448 × 504 was first modeled, with 6720 cells in the metal region and 13692 cells in the green region.

The ambient temperature was set to 0°C. Thermal conductivities of FR-4 and copper were respectively set to 0.3W/mK and 400W/mK the same as given in COMSOL. $h_{e,ac}$ was set to 0.01 W/m^{2}K. 200 groups of eigenvalues were set, and further increasing the number of eigenvalues changed little the hotspot temperature.

The model was analyzed under two different cases, with or without the calculation of the heat spreading in the metal layer. The case "without the metal layer" can be used for testing the iterative method when only the analytical solution was solved. The case "with the metal layer" can be used for testing both the iterative method and the numerical-analytical coupling strategy.

In COMSOL, the 'General Heat Transfer' module was used to model the 3D structure. A fine mesh was obtained with 80,492 elements in the structure and 4230 elements in the heating region. Further refining the mesh generated little difference in the results.

The simulated temperature maps of the heating region under two cases are shown in Fig. 9 and Fig. 10 respectively. For the case "without the metal layer", both the color-scale maps of temperature from two programs are quite consistent. Two curves of the temperature along the line x = 0.033m in the yellow region are overlapping to each other. The differences between them are negligible.

For the case "with the metal layer", the heat-spreading analysis of the metal layer was included. By analyzing the data of those two curves shown in Fig.10(e), along the line

$$\begin{cases} T_{M,u} = R_{Mu,Mu}q_{M,u} + R_{Mu,Md}q_{M,d} + R_{Mu,Iu}q_{ex-r,Iu} + R_{Mu,Id}q_{ex-r,Id} \\ T_{M,d} = R_{Md,Mu}q_{M,u} + R_{Md,Md}q_{M,d} + R_{Md,Iu}q_{ex-r,Iu} + R_{Md,Id}q_{ex-r,Id} \\ T_{I,u} = R_{Iu,Mu}q_{M,u} + R_{Iu,Md}q_{M,d} + R_{Iu,Iu}q_{ex-r,Iu} + R_{Iu,Id}q_{ex-r,Id} \\ T_{I,d} = R_{Id,Mu}q_{M,u} + R_{Id,Md}q_{M,d} + R_{Id,Iu}q_{ex-r,Iu} + R_{Id,Id}q_{ex-r,Id} \\ M_{M,u}T_{M,u} - M_{V,d}T_{M,d} = q_{MJ,u} - q_{M,u} \\ M_{M,d}T_{M,d} - M_{V,u}T_{M,u} = q_{MJ,d} - q_{M,d} \\ q_{MJ,u} = q_{P,u} + M_{R,u}T_{M,u} + M_{Hdif,Mu}T_{M,u} \\ q_{MJ,d} = q_{P,d} + M_{R,d}T_{M,d} + M_{Hdif,Md}T_{M,d} \\ q_{ex-r,Iu} = M_{Hdif,Iu}T_{I,u} \\ q_{ex-r,Id} = M_{Hdif,Id}T_{I,d} \end{cases} \tag{28}$$

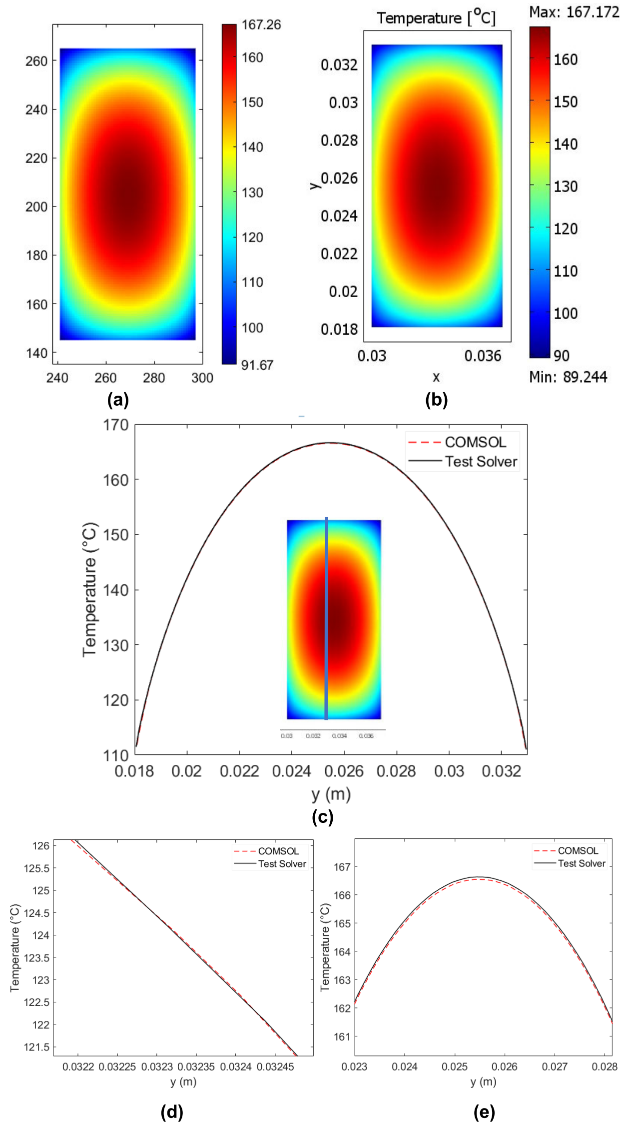

FIGURE 9. Comparison of the temperature map of the heating region without the metal layer: (a) Test solver, (b) COMSOL, (c) Comparison of the temperature along the line of x = 0.033mm, (d) Zoom-in figure of (c) around y = 0.0324mm, (e) Zoom-in figure of (c) around y = 0.0255mm.

of x = 0.033m, the maximum absolute difference of temperature is about 0.41°C, and the average is about 0.36°C. For further deriving the accuracy based on Richardson's extrapolation [15], the models under other two layout resolutions were also built. The precondition to approximately derive the error is the monotone convergence of the results under three consecutive grid densities. Then the exponent relating to the error can be computed through the following logarithmic calculation with e base from the results of three consecutive grids [15]:

$$p = \frac{\log(\frac{\phi_{2l_c} - \phi_{4l_c}}{\phi_{l_c} - \phi_{2l_c}})}{\log 2} \tag{29}$$

in which, ϕ_{lc}, ϕ_{2lc}, and ϕ_{4lc} refer to the solutions under three cell lengths of l_c, $2l_c$, and $4l_c$ respectively. Then the error of ϕ_{lc} can be approximately derived:

$$\varepsilon_{l_c} \approx \frac{\phi_{l_c} - \phi_{2l_c}}{2^p - 1} \tag{30}$$

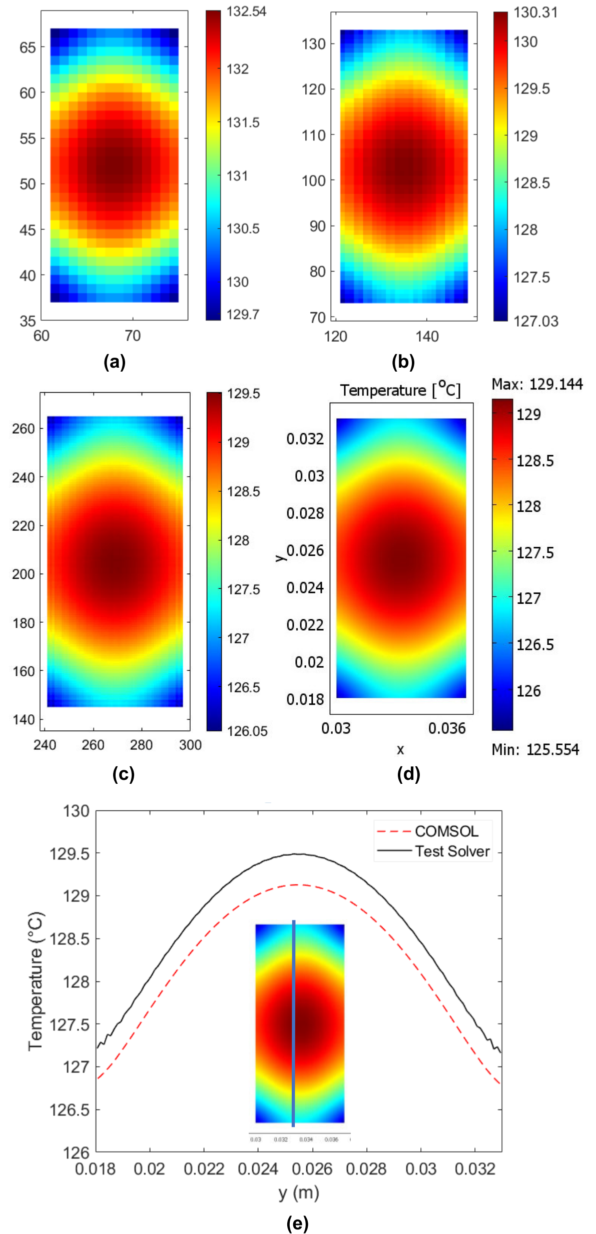

FIGURE 10. Comparison of the temperature maps of the heating region with the metal layer: (a) under 112 × 126 layout from the test solver (b) under 224 × 252 layout from the test solver, (c) under 448 × 504 layout from the test solver, (d) COMSOL, (e) Comparison of the temperature along the line of x = 0.033mm between the results of (c) and (d).

Based on the first three maps shown in Fig.10, the error of the hotspot temperature under the resolution 448 × 504 is about −0.45°C. Thus, the approximate hotspot temperature is about 129.05°C and its difference from that of COMSOL is quite small. Hence, integrating the iterative method for radiation heat transfer in the coupling method is feasible.

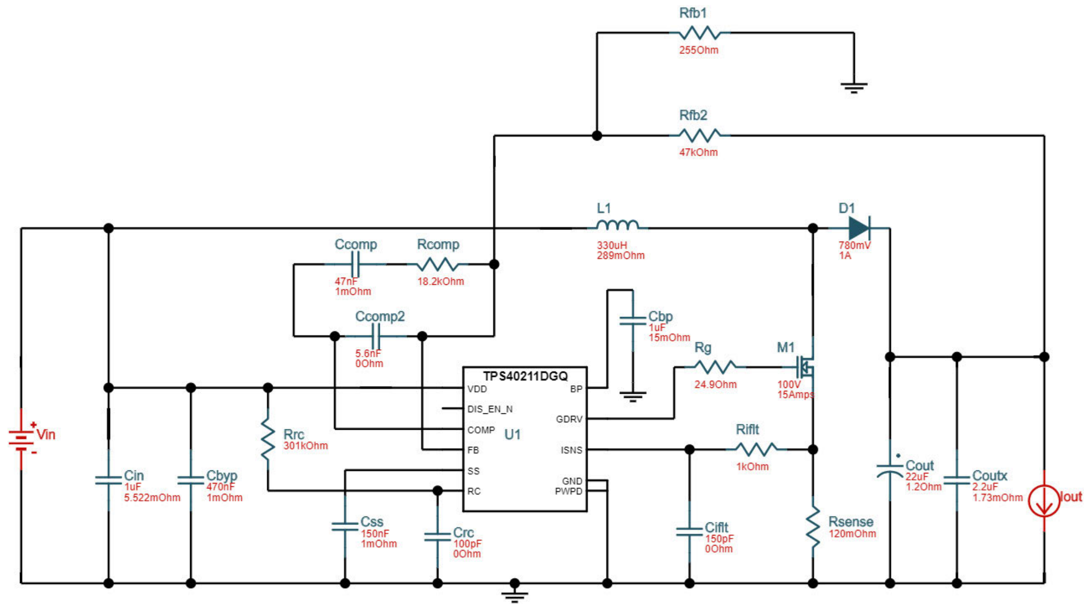

FIGURE 11. Circuit schematic of the DC-DC power supply.

VII. THE MODEL OF A PHANTOM POWER-SUPPLY PCB

A. PARAMETERS

The PCB of a phantom DC-DC power supply for microphones was modeled in the test solver as well. The input range of the circuit is from 9V to 13V, and the output is 48V. The circuit and PCB layout shown in Fig. 11 and Fig. 12 were automatically generated by the online tool TI WEBENCH@Power Supply. Besides, the bill of materials, characteristic charts, and components' dissipating power can be also obtained from the online tool.

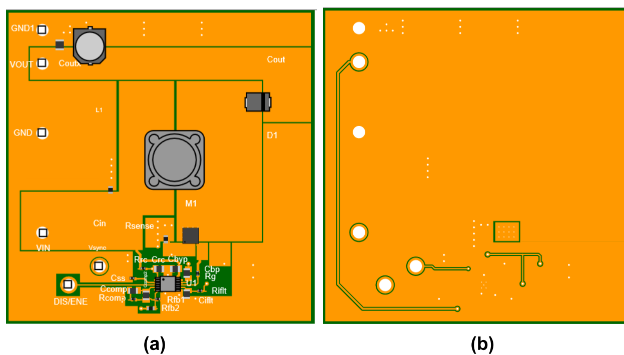

FIGURE 12. Layout maps of the power-supply PCB generated from the online tool: (a) Top side, (b) Bottom side.

The layout maps of the two-layer PCB were originally generated in the size of 62.5mm × 64mm. Then in order to have a more compact dimension, the size of the PCB was further reduced to 37.6mm × 47.6mm as shown in Fig. 13. The resolution of the layout map is 376 × 476, thus the unit length of one pixel is 0.1mm. Under the one-level uniform grid there are totally 142300 and 159568 cells in the metal layers on the top and bottom sides respectively.

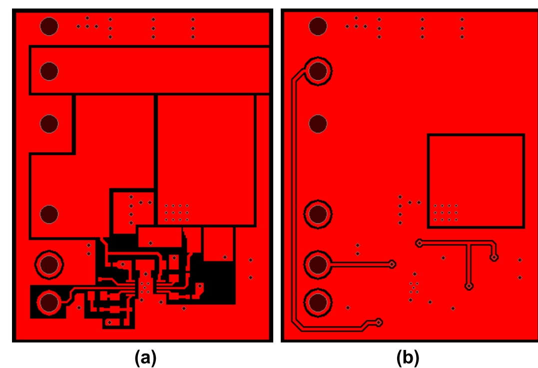

FIGURE 13. Compact layout maps of the power-supply PCB: (a) Top metal layer, (b) Bottom metal layer.

After applying the three-level multigrid, the number of metal cells reduced to 35722 and 15937 each. Fig. 14 shows the discrete-cell maps of the metal layer on both sides with yellow level-3 cells (biggest), green level-2 cells, and blue level-1 cells (smallest). Under such three-level multigrid, only for the calculation of the heat spreading in two metal layers as shown in (12), the number of product operation of matrix elements can decrease from 1.8225^{11} $(2(142300+159568)^2)$ to 5.3373^9 $(2(35722+15937)^2)$, about 97% decrements. Obviously, the operation burden for preparing all the matrix coefficients in the group of equations can be reduced significantly as well.

There are 21 components in the PCB. Table 1 shows their parameters of the thermal resistance as well as the dissipating power under 11V input and 48V/0.05A output. For the controlling IC *U1*, both $R_{\theta JC}$ and $R_{\theta JC(top)}$ are given in the datasheet. For the MOSFET *M1* and diode *D1*, in the datasheets only the corresponding $R_{\theta JC}$ are given, so their $R_{\theta JC(top)}$ were conservatively assumed as the thermal

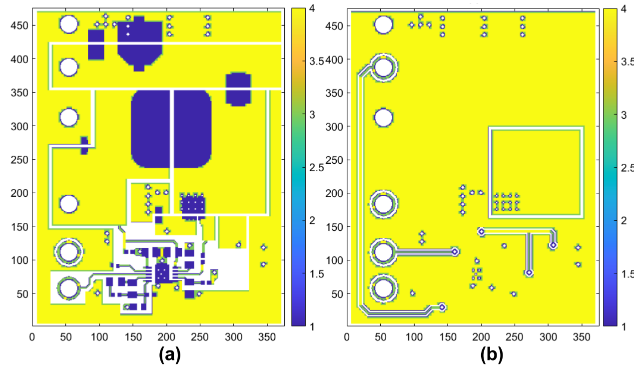

FIGURE 14. Discrete-cell maps of the metal layers under the three-level multigrid: (a) Top metal layer, (b) Bottom metal layer.

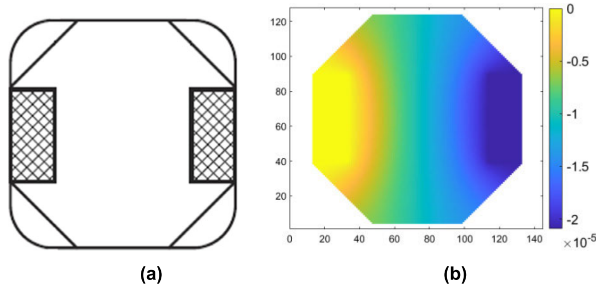

FIGURE 15. (a) Schematic of L1's bottom side, (b) Analog distribution of electrical potential (V) of the insulating material between two pads.

resistance from the top to the bottom of the device by using the thermal conductivity of the general packaging mold compound 0.63W/mK [27].

For the SMD inductor *L1*, Coilcraft Inc. has announced that since this kind of inductor has a variety of thermal flow paths and multiple heat sources (the winding and core), there is not a definite junction inside and the parameters relating to thermal resistance are usually not supported [28]. On the other hand, due to the existence of the insulating coating material over the winding wire as well as the possible space between the winding and core, the thermal conduction through them is hard to be scaled, so that $R_{\theta JC(top)}$ of *L1* was first assumed to be infinity.

However, two pads of the inductor *L1* are connected by both the metal windings and the insulating material of the package as shown in Fig. 15. Hence, at least the thermal resistance between two pads can be conservatively estimated by analyzing these two parts. The dimension of the inductor is 12mm × 12mm and the thickness of the insulating part between two pads is 0.635mm. The thermal resistance of this part was analyzed in the test solver by running the program of calculating the electrical potential distribution of the metal layer.

Fig. 15(b) shows the simulated distribution of the electrical potential under the assumed 1A current and 1.72×10^{-8}S/m electrical conductivity. The analog electrical resistance $2.09 \times 10^{-5}\Omega$ was derived, thus the thermal resistance 1928°C/W was further derived with the thermal conductivity 0.63W/mK of the general packaging mold compound. On the other hand, the equivalent thermal resistance of the copper winding ($R_{DC} = 0.289\Omega$) was more than 42000°C/W, so its thermal-conduction contribution was neglected. The middle plane of the insulating material between two pads was assumed as the virtual junction region, thus *L1's* $R_{\theta JC}$ was assumed to be 482 °C/W (one fourth of 1928 °C/W), as the thermal resistance from two pads to the middle plane.

TABLE 1. Type, dissipating power P_d, $R_{\theta JC}$ and $R_{\theta JC(top)}$ of the components.

Components (Type)	P_d(mW)	$R_{\theta JC}$(°C/W)	$R_{\theta JC(top)}$(°C/W)
M1 (CSD19538Q3A)	338.07	5.5	153.6
U1 (TPS40211DGQR)	57.33	15.6	50.5
R_{fb2} (RC0603FR-0747KL)	48.76	63	0
D1 (10BQ100TRPBF)	25.9	22	235.8
L1 (MSS1210-334KEB)	16.98	482	——
C_{out} (EEE-FK1J220XP)	0.366	2.47	0
C_{outx}(C3225X7R2A225K230AB -1210)	0.008	6.85	0
C_{in} (C1608X7R1V105K080AC -0603)	0.001	30.89	0
C_{iflt} (CL21C151JBANNNC-0805)	0	27.18	0
C_{bp} (C0805C105K4RACTU -0805)	0	17.79	0
C_{ss} (GRM155R61A154KE19D -0402)	0	60.92	0
C_{comp2}(CGA4C2C0G1H562J060AA -0805)	0	22.83	0
C_{comp} (GRM21BR72A473KA01L -0805)	0	20.80	0
C_{rc} (CL21C101JBANNNC -0805)	0	27.71	0
C_{byp} (TMK212BJ474KD-T -0805)	0	18.45	0
R_{iflt} (CRCW04021K00FKED -0402)	0	90	0
R_{comp} (CRCW040218K2FKED -0402)	0	90	0
R_{rc} (CRCW0402301KFKED -0402)	0	90	0
R_g (CRCW040224R9FKED -0402))	0	90	0
R_{fb1} (CRCW0402255RFKED -0402)	0	90	0
R_{sense}(ERJ-3RSFR12V-0603)	0	63	0

The thermal resistance $R_{\theta JC}$ for SMD resistors can be found in a report from Vishay [29], which has listed such parameters under different sizes. $R_{\theta JC(top)}$ for each SMD resistor was approximately neglected due to their slim structures and small size.

$R_{\theta JC}$ for each SMD ceramic capacitor cannot be found in the datasheet but was roughly estimated based on ATC's technical report [30]. Based on the internal multi-layer structure of the capacitor, the thermal resistance Θ_{cap} between the middle heat-generation plane and two pads was analyzed [30]. The assumption of the heat-generation plane implied the ignorance of $R_{\theta JC(top)}$ of the SMD ceramic capacitor. Several capacitors of series 100A and 100B from ATC were analyzed [30], and their structure parameters and Θ_{cap} are reproduced in Table 2.

TABLE 2. Capacitor parameters in ATC's report [30] and estimated k_{cap}.

Series	100A		100B		
Capacitance (pF)	1	100	1	100	1000
Length (mm)	1		2.2		
A_{cap} (mm^2)	2		7		
Θ_{cap} (°C/W)	13.7	11.4	7.9	7.2	5.9
k_{cap} (W/mmK)	0.0091	0.0110	0.0099	0.0109	0.0133

The equivalent thermal conductivity of the capacitor k_{cap} was derived for each capacitor shown in the table. Between the capacitance and k_{cap}, there seems to be a relation that k_{cap} changes not much under different size with the same capacitance. Then, by using the Curve Fitting Tool of MATLAB, the approximate relation between k_{cap} and the capacitance (nF) can be derived:

$$k_{cap} \approx 0.0129C^{0.04809} \tag{31}$$

Such inference was further used for estimating $R_{\theta JC}$ of the ceramic capacitors in the power-supply PCB.

C_{out} is an electrolytic capacitor, of which the inner vertical (axial) thermal conductivity (about 100 W/mK) is much larger than the radial (about 0.21 W/mK) [31] due to its multilayer-wrapped electrode structure inside. Hence, $R_{\theta JC}$ and $R_{\theta JC(top)}$ of the electrolytic capacitor can be approximately derived by only analyzing the vertical thermal conduction. As shown in the thermal analysis of an electrolytic capacitor with the power loss between 0.2W and 1.2W under the air velocity between 0 and 1m/s [32], the temperature difference between the top case and core was always less than 1°C, thus the top case was considered as the best point to reflect the electrolytic capacitor's core temperature. Hence, $R_{\theta JC(top)}$ of C_{out} can be also approximately neglected.

The power-supply PCB was modeled and simulated under the similar boundary conditions as the one-layer structure model discussed in Section VI. The group number of eigenvalues was set to 200 as well. Radiation from the top side was considered as the only way of heat transfer between the board and the ambient. As introduced in Section VI, the emissivity can be approximately set to 0.9 for both the epoxy-based solder mask [5] and the plastic package material of ICs [25], [26]. Thus, the emissivities of M1, D1 and U1 were also set to 0.9. According to the emissivity measurement of several kinds of components, the average emissivity of each kind of component was calculated [26]. Hence, based on the average [26], the emissivities of the electrolytic capacitor and SMD resistors were set to 0.88, and that of the ceramic capacitor was set to 0.94.

B. MODELING RESULTS

The temperature maps of 376 × 476 resolution for both the top and bottom sides under the ambient temperature (T_a) of 20°C are shown in Fig. 16. The junction temperature T_J and maximum pad temperature T_{pad_max} of each component at different T_a are listed in Table 3.

TABLE 3. T_J and T_{pad_max} of components at different T_a.

Components	$T_a = 0$ °C		$T_a = 20$ °C		$T_a = 40$ °C	
	T_J(°C)	T_{pad_max} (°C)	T_J(°C)	T_{pad_max} (°C)	T_J (°C)	T_{pad_max} (°C)
M1	69.21	68.19	81.42	80.40	94.79	93.77
U1	57.09	57.23	69.32	69.46	82.73	82.87
R_{fb2}	65.86	63.09	78.10	75.33	91.50	88.73
D1	56.20	57.10	68.44	69.33	81.85	82.73
L1	64.07	60.08	76.32	72.30	89.73	85.69
C_{out}	51.53	51.63	63.80	63.90	77.25	77.35
C_{outx}	51.03	51.13	63.31	63.41	76.76	76.86
C_{in}	51.72	51.92	63.99	64.19	77.43	77.63
C_{iflt}	55.11	55.35	67.35	67.59	80.75	80.99
C_{bp}	55.81	55.86	68.04	68.09	81.44	81.49
C_{ss}	53.27	53.56	65.53	65.81	78.95	79.24
C_{comp2}	56.14	56.58	68.38	68.81	81.78	82.22
C_{comp}	55.35	55.54	67.60	67.78	81.00	81.19
C_{rc}	55.27	55.55	67.51	67.79	80.93	81.20
C_{byp}	55.54	55.65	67.77	67.88	81.18	81.29
R_{iflt}	55.06	55.10	67.30	67.33	80.70	80.73
R_{comp}	55.56	55.84	67.80	68.08	81.21	81.49
R_{rc}	54.37	54.78	66.61	67.02	79.93	80.43
R_g	58.28	59.09	70.50	71.31	83.79	84.70
R_{fb1}	56.90	58.55	69.13	70.79	82.53	84.19
R_{sense}	57.87	60.43	70.10	72.65	83.51	86.04

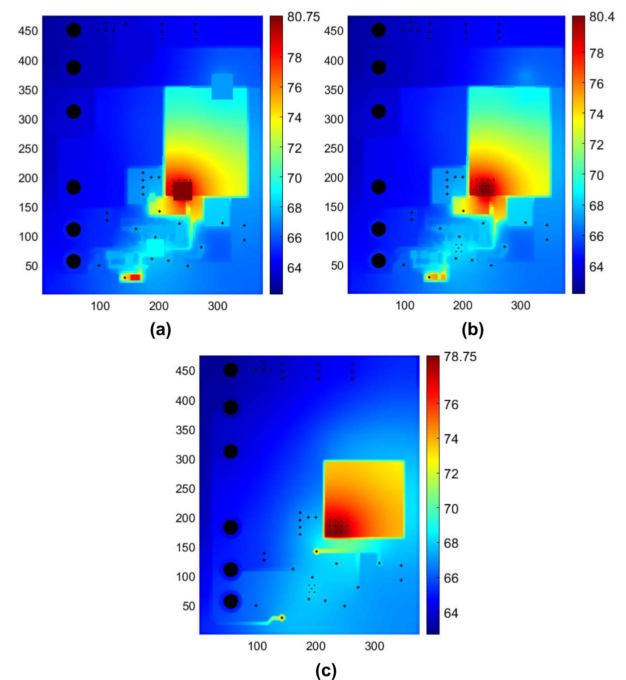

FIGURE 16. Temperature maps of the PCB of the phantom power supply at $T_a = 20$°C: (a) Top side, (b) Top layer surface, (c) Bottom side.

During the iteration, $h_{e,ac}$ was set to 0.01 W/mK. The temperature arrays under three ambient temperatures all converged to the last results after 9 rounds of iteration. In the end of the iteration, firstly the total heating power of the components can be calculated by using the relations given in Section IV to testify its consistency to the total setting dissipation power 487.415mW. Based on components' thermal-resistance parameters, junction and case-top temperatures, pad-cell temperatures and the radiation-equivalent

HTC, the total heating power of the components was all approximately equal to 487.415mW under each case of T_a with only tiny difference less than 10^{-10} mW. Second, the total rate of radiation heat transfer can be also calculated based on the temperature map of the top side. Under each case of T_a, the total radiation rate was all between 487.1mW and 487.3mW. The little difference from 487.415mW is partly due to the little error of the radiation-equivalent HTC. The other reason is the application of the three-level multigrid, because the temperatures of the level-3 cell and level-2 cell approximately represent the temperatures of the corresponding 16 cells and 4 cells respectively.

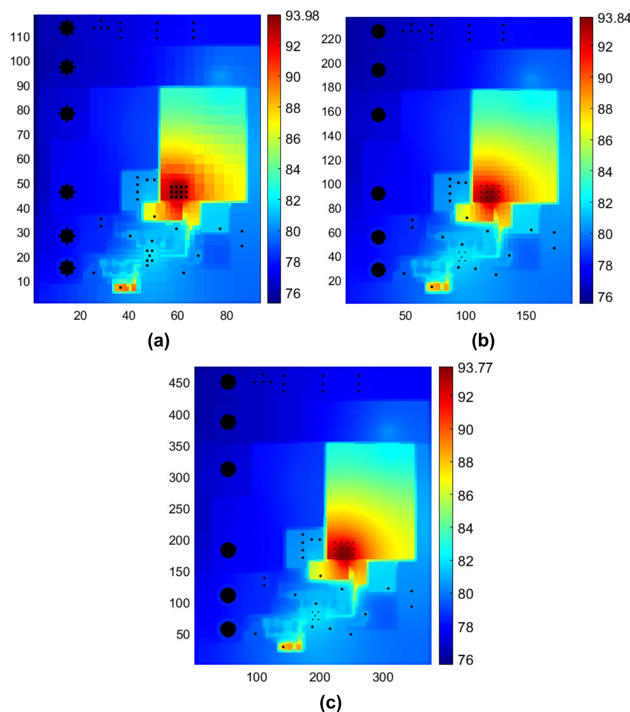

FIGURE 17. Temperature maps of the top layer surface at $T_a = 40°C$ under three resolutions: (a) 94 × 119, (b) 188 × 238, (c) 376 × 476.

For deriving the accuracy of the model based on Richardson's extrapolation, the layout maps were also modeled and analyzed under other two resolutions, 94 × 119 and 188 × 238. The temperature maps of the top layer surface obtained under each resolution at $T_a = 40°C$ are shown in Fig. 17. The similar distributions and little differences between the temperature results under three discrete densities further testify the consistency, stability, and convergence [15] of the proposed method.

The junction temperature of the MOSFET T_{J_M1}, the maximum temperature in the top metal layer T_{M_max}, and the minimum cell length $l_{c,min}$ under each resolution are listed in Table 4. The error of T_{M_max} based on Richardson's extrapolation under the resolution 376 × 476 is about −0.0882°C, thus the approximate value of T_{M_max} is about 93.69°C. Since the difference between T_{J_M1} and T_{M_max} is close to 1°C, the approximate value of T_{J_M1} is about 94.69°C.

TABLE 4. T_{M_max} and T_{J_M1} at $T_a = 40°C$ under three resolutions.

Map Resolution	94 x 119	188 x 238	376 x 476
$l_{c,min}$ *(mm)*	0.4	0.2	0.1
T_{J_M1} (°C)	94.9703	94.8725	94.7909
T_{M_max} (°C)	93.9878	93.8498	93.7751

As assumed before, the radiation from the inductor was ignored. In order to test the possible influence of such ignorance, the radiation from the inductor was taken into account by assuming zero $R_{\theta JC(top)}$ of the inductor. The simulated temperature maps are shown in Fig. 18.

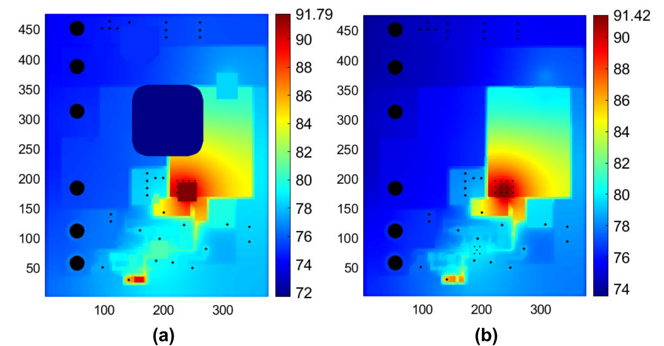

FIGURE 18. Temperature maps at $T_a = 40°C$ with assumed zero $R_{\theta Jtop}$ of the inductor: (a) Top side, (b) Top layer surface.

Under the assumption of zero $R_{\theta JC(top)}$ of the inductor, its top surface temperature is close to 72°C. Moreover, the error of T_{M_max} is about −0.22°C and its approximate value is about 91.20°C. Hence, under those assumed components' thermal parameters and boundary conditions, neglecting the radiation from the inductor does not generate large error in the hotspot temperature, even though the inductor has a big surface. This could be mainly due to the much lower dissipation power of the inductor.

According to upper modeling results, the radiation from the components is about between 6% and 13% of the total radiation under each case of boundary conditions, whereas the percentage of the radiation from the metal layer region is about more than 70%. Obviously, the heat-spreading contribution of the metal layer is significant. Hence, the PCB should not be designed by only considering compactness, but sometimes the surface area should be left big enough for heat spreading and the heat transfer between the PCB and the ambient.

On the other hand, T_J of some components are lower than their T_{pad_max}. This is because these components can be mainly considered as thermal-conduction paths rather than heating sources, especially those without heat dissipation or with relatively low thermal resistance and much lower dissipation power.

VIII. CONCLUSION

The numerical-analytical coupling method for steady-state thermal analysis of the PCB has been further improved to

include the analysis of radiation heat transfer, predict the temperature information of components, and consider the reality of components' coverage on the PCB surface. Instead of the one-level uniform grid, the multigrid strategy has been applied for generating discrete cells of three levels, and the operation burden can be decreased significantly. By using components' $R_{\theta JC}$ and $R_{\theta JC(top)}$, their junction temperatures and average case-top temperatures can be correlated with the temperature distribution of the layer surface. Finally, the laminated structure and components of the PCB as a whole can be thermally modeled. The numerical-analytical modeling strategy may be possible to be used for the analysis of other engineering problems.

Radiation heat transfer has been correlated with the radiation-equivalent heat transfer coefficient of each discrete cell and component's case top in the proposed iterative method. Based on the little difference of the modeling results between the test solver and COMSOL for a simple one-layer structure, the mechanism of the iterative method has been testified to be feasible. The iterative method may be further used for solving other temperature-dependent heat transfer problems.

Based on the modeling results of the phantom DC-DC power supply PCB, the consistency, stability, convergence, and conservation of the improved modeling method has been further verified. Certainly, if the manufacturers of components declare thermal parameters more clearly and comprehensively, the thermal model of the PCB can be built more accurately. The components with lower thermal resistance and much lower dissipation power can be mainly considered as the thermal-conduction paths contributing to the heat spreading in the PCB. On the other hand, the heat spreading of the metal layers in the PCB can be significant, and the PCB surface may contribute most to the radiation heat transfer compared to the components. Hence, squeezing the size of the PCB may not only depend on electrical design rules of the layout, but also thermal analysis.

REFERENCES

[1] T. F. Lemczyk, B. L. Mack, J. R. Culham, and M. M. Yovanovich, ''PCB trace thermal analysis and effective conductivity,'' *J. Electron. Packag.*, vol. 114, no. 4, pp. 413–419, Dec. 1992, doi: 10.1115/1.2905474.

[2] J. R. Culham and M. M. Yovanovich, ''Factors affecting the calculation of effective conductivity in printed circuit boards [thermal analysis],'' in *Proc. ITherm*, Seattle, WA, USA, 1998, pp. 460–467.

[3] M. B. Dogruoz and G. Shankaran, ''Spatial variation of temperature on printed circuit boards: Effects of anisotropic thermal conductivity and Joule heating,'' *IEEE Trans. Compon., Package., Manuf. Technol.*, vol. 2, no. 10, pp. 1649–1658, Oct. 2012, doi: 10.1109/TCPMT.2012.2205251.

[4] M. B. Dogruoz, ''Assessment of Joule heating and temperature distribution on printed circuit boards Via electrothermal simulations,'' *J. Electron. Packag.*, vol. 138, no. 2, pp. 1–8, Jun. 2016, doi: 10.1115/1.4033109.

[5] Y. Shen, H. Wang, F. Blaabjerg, H. Zhao, and T. Long, ''Thermal modeling and design optimization of PCB vias and pads,'' *IEEE Trans. Power Electron.*, vol. 35, no. 1, pp. 882–900, Jan. 2020, doi: 10.1109/TPEL.2019.2915029.

[6] A. Ali, K. Ullah, H. U. Rehman, I. Bari, and L. M. Reyneri, ''Thermal characterisation analysis and modelling techniques for CubeSat-sized spacecrafts,'' *Aeronaut. J.*, vol. 121, no. 1246, pp. 1858–1878, Dec. 2017, doi: 10.1017/aer.2017.108.

[7] A. Ali, J. Tong, H. Ali, M. R. Mughal, and L. M. Reyneri, ''A detailed thermal and effective induced residual spin rate analysis for LEO small satellites,'' *IEEE Access*, vol. 8, pp. 146196–146207, 2020, doi: 10.1109/ACCESS.2020.3014643.

[8] B. Blackmore, ''Validation and sensitivity analysis of an image processing technique to derive thermal conductivity variation within a printed circuit board,'' in *Proc. 25th Annu. IEEE Semiconductor Thermal Meas. Manage. Symp.*, San Jose, CA, USA, Mar. 2009, pp. 76–86.

[9] P. Blais and A. Munyaneza, ''PCB thermal modeling with empirical thermal conductivity methods,'' Mentor Graph. Corp., Wilsonville, OR, USA, Tech. Rep. TECH17480, 2018.

[10] X. Song, V. Pickert, B. Ji, R. T. Naayagi, C. Wang, and Y. Yerasimou, ''Questionnaire-based discussion of finite element multiphysics simulation software in power electronics,'' *IEEE Trans. Power Electron.*, vol. 33, no. 8, pp. 7010–7020, Aug. 2018.

[11] P. E. Bagnoli and Y. Zhang, ''Electro-thermal simulation of metal interconnections under high current flow,'' *Microelectron. Rel.*, vol. 50, nos. 9–11, pp. 1672–1677, Sep. 2010, doi: 10.1016/j.microrel.2010.07.029.

[12] Y. Zhang, A. Pennatini, and P. E. Bagnoli, ''A thermal model for the PCB structure including thermal contribution of traces and vias,'' in *Proc. 18th THERMINIC*, Budapest, Hungary, 2012, pp. 105–110.

[13] Y. Zhang, ''Modeling methodology for reliability-concerned current density analysis of PCB tracks and thermal analysis of PCB structure,'' Ph.D. dissertation, Dept. Inf. Eng., Univ. Pisa, Pisa, Italy, 2013.

[14] Y. Zhang and P. E. Bagnoli, ''A modeling methodology for thermal analysis of the PCB structure,'' *Microelectron. J.*, vol. 45, no. 8, pp. 1033–1052, Aug. 2014, doi: 10.1016/j.mejo.2014.04.042.

[15] H. J. Ferziger and M. Peric, ''Efficiency and accuracy improvement,'' in *Computational Methods for Fluid Dynamics*, 3rd ed. Berlin, Germany: Springer-Verlag, 2002, pp. 329–364.

[16] H. K. Versteeg and W. Malalasekera, ''The finite volume method for convection-diffusion problems,'' in *An Introduction to Computational Fluid Dynamics—The Finite Volume Method*, 2nd ed. Edinburgh Gate, U.K.: Pearson, 2007, pp. 134–176.

[17] P. E. Bagnoli, C. Bartoli, and F. Stefani, ''Validation of the DJOSER analytical thermal simulator for electronic power devices and assembling structures,'' *Microelectron. J.*, vol. 38, no. 2, pp. 185–196, Feb. 2007, doi: 10.1016/j.mejo.2006.10.001.

[18] P. E. Bagnoli and F. Stefani, ''Electrothermal simulation of the hot-spot and its countermeasures in cellular bipolar power transistors,'' *IEEE Trans. Compon. Packag. Technol.*, vol. 32, no. 2, pp. 493–500, Jun. 2009, doi: 10.1109/TCAPT.2008.2001193.

[19] K. R. Choudhury and J. D. Rogers, ''Steady-state thermal modeling of a power module: An *N*-layer Fourier approach,'' *IEEE Trans. Power Electron.*, vol. 34, no. 2, pp. 1500–1508, Feb. 2019, doi: 10.1109/TPEL.2018.2828439.

[20] K. R. Bagnall, Y. S. Muzychka, and E. N. Wang, ''Analytical solution for temperature rise in complex multilayer structures with discrete heat sources,'' *IEEE Trans. Compon., Package., Manuf. Technol.*, vol. 4, no. 5, pp. 817–830, May 2014, doi: 10.1109/TCPMT.2014.2299766.

[21] S. Luhar, D. Sarkar, and A. Jain, ''Steady state and transient analytical modeling of non-uniform convective cooling of a microprocessor chip due to jet impingement,'' *Int. J. Heat Mass Transf.*, vol. 110, pp. 768–777, Jul. 2017, doi: 10.1016/j.ijheatmasstransfer.2017.03.064.

[22] P. Li, L. T. Pileggi, M. Asheghi, and R. Chandra, ''IC thermal simulation and modeling via efficient multigrid-based approaches,'' *IEEE Trans. Comput.-Aided Design Integr. Circuits Syst. Circuits Syst. Circuits Syst.*, vol. 25, no. 9, pp. 1763–1766, Sep. 2006, doi: 10.1109/TCAD.2005.858276.

[23] S. Abdelkader and A. E. El-Rouby, ''Power-aware meshing algorithm for thermal analysis of integrated circuits,'' *IEEE Trans. Compon., Packag., Manuf. Technol.*, vol. 6, no. 9, pp. 1340–1348, Sep. 2016, doi: 10.1109/TCPMT.2016.2598882.

[24] D. Edwards and H. Nguyen, ''Semiconductor and IC package thermal metrics,'' Texas Instrum., Dallas, TX, USA. App. Rep., SPRA953C, Dec. 2003.

[25] (Mar. 2018). *FLIR*. [Online]. Available: https://flir.custhelp.com/app/answers/detail/a_id/1281/~/emissivity-settings-when-imaging-pcbs-and-electronics/session/L2F2LzEvdGltZS8xNjE3ODgwMDkzL2dlbi8xNjE3ODgwMDkzL3NpZC9mVXFBZnZNOVZXa0dEUk5yWm80MW41QVd0ZU1NdzZyUjI2cGgydEJCdkU0R1lEOGJxMDdhYTVFQmlJTmxCbjg0JTdFMkRlQUtFVmJoeUhXNUhvTHZnRGhxUTglN0VzOENJRDU1Vk5pb2JIOUtMUjJKRDE3RU10WVA0bnFBJTIxJTIx

[26] P. Svasta, D. Simion-Zanescu, and R. Ionescu, "Components' emissivity in reflow soldering process," in *Proc. 54th Electron. Compon. Technol. Conf.*, Las Vegas, NV, USA, Jun. 2004, pp. 1921–1924.
[27] N. Bhandarkar, S. Mhaisalkar, P. Lee, and D. Tracy, "Effect of package construction on thermal performance of plastic IC packages," in *Proc. 1st Electron. Packag. Technol. Conf.*, Singapore, Oct. 1997, pp. 65–68.
[28] Coilcraft. *Why Don't You Specify Thermal Resistance for Your Products?* Accessed: Aug. 2020. [Online]. Available: https://www.coilcraft.com/en-us/faq/
[29] *Thermal Management in Surface-Mounted Resistor Applications*, Vishay Intertechnology, Malvern, PA, USA, Appl. Note 28844, Feb. 2011.
[30] F. M. Schabauer and R. Blumkin, "Thermal resistance, power dissipation and current rating for ceramic and porcelain multilayer capacitors," Amer. Tech. Ceram. (Florida), Jacksonville, FL, USA, Tech. Rep. ATC 001-867, 1981.
[31] S. G. Parler, "Thermal modeling of aluminum electrolytic capacitors," in *Proc. Conf. Rec. IEEE Ind. Appl. Conf. 34th IAS Annu. Meeting*, Phoenix, AZ, USA, Oct. 1999, pp. 2418–2429.
[32] Z. Na, "A study of electrolytic capacitor thermal conductivity, behavior & measurement," in *Proc. 22nd Int. Workshop Thermal Invest. ICs Syst. (THERMINIC)*, Budapest, Hungary, 2016, pp. 315–318. [Online]. Available: https://ieeexplore.ieee.org/abstract/document/7749074

YABIN ZHANG received the B.S. degree in electrical engineering from the Dalian University of Technology, Dalian, China, in 2003, the M.S. degree in radiation protection from the Graduate School, China Academy of Engineering Physics, Beijing, China, in 2006, and the Ph.D. degree in information engineering from the University of Pisa, Italy.

Since November 2017, he has been with Xihua University, Chengdu, China, where he is currently a Senior Researcher with the School of Electrical Engineering and Electronic Information. He was ever working as a Research Assistant with the China Academy of Engineering Physics, the Laboratory of Power Electronics, University of Pisa, and the Innovation Laboratory of Cubit Scarl, Pisa, Italy. He published several articles in the field of thermal modeling and simulation method of the PCB. He also holds three pending patents about the thermal-modeling method of the PCB. His current research interests include thermal modeling methods and algorithm optimization.